Session VI, Tuesday, June 20, afternoon

L16

DIFFRACTION SURFACES IN X-RAY CRYSTAL MONOCHROMATORS PREPARED BY NANO-MACHINING TECHNIQUE

Z. Zápražný[1], D. Korytár[1], Y. Halahovets[2], M. Jergel[2], C. Ferrari[3], J. Hagara[1,4], E. Dobročka[1]

[1]Institute of Electrical Engineering, Slovak Academy of Sciences, Dúbravská cesta 9, 841 04 Bratislava, Slovakia

[2]Institute of Physics, Slovak Academy of Sciences, Dúbravská cesta 9, 845 11 Bratislava, Slovakia

[3]CNR-IMEM Institute, Parco Area delle Scienze 37/A, 431 24 Parma, Italy

[4]Integra TDS s. r. o., Pod Párovcami 4757/25, 921 01 Pieš any, Slovakia

zdenko.zaprazny@savba.sk

We study and develop methods for producing diffraction surfaces in X-ray crystal monochromators using advanced deterministic nano-machining technique [1]. Nano-machining uses a single point diamond tool to remove material from the surface. We have adopted two kinds of nano-machining techniques: Single point diamond turning (SPDT) and Fly cutting (grooving). The techniques are well developed for producing surfaces of infrared or visible light optics [2], however, their implementation for hard X-ray optics is a very challenging task. In a so called ductile mode, this technology is applicable even to brittle materials like germanium or silicon that are difficult to be machined, being only little invasive to crystal lattice beneath the surface. In particular, high-resolution TEM images have revealed absence of any dislocations in the subsurface region of the nano-machined Ge samples in the case of feed rate of 0.125 mm/min (Fig. 1).

The crucial parameter is the surface roughness. The diamond tool produces periodical surface ripples, which can cause e.g. unwished parasitic interference effects in the case of hard X-ray radiation. HRXRD measurements showed that the periodicity of the ripples can vary from 700 to 40 nm depending on the used feed rate of nano-machining. Figure 2 shows a setup for the reciprocal space map (RSM) measurement of the Ge machined samples and channel-cut monochromator shown in Figure 3. The feed rate of nanomachining was 1 mm/min and the sample exhibits ripples with 416 nm periodicity (Figure 4). We have obtained very low surface roughness by optimizing of machining parameters and slowing down the feed rate to lower value of 0.125 mm/min. The truncation rods in reciprocal map were suppressed remaining only diffuse scattering indicating that the period of ripples after the tool is too short to observe using this HRXRD setup (Figure 5). By using of additional chemo-mechanical post-polishing process we have achieved the surface roughness (RMS) in the range of 1 - 0.3 nm according to AFM measurements. Applying SPDT nano-machining, it is possible to produce not

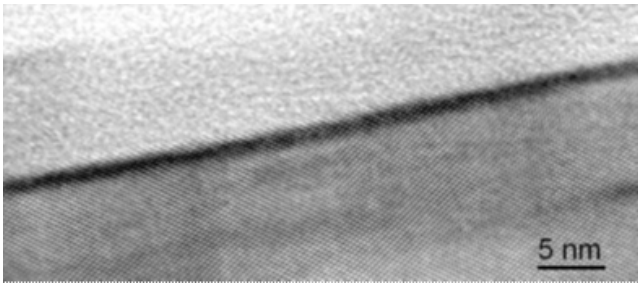

Figure 1. HR TEM image shows that the top surface is not perfectly flat as some valleys and crests of a few atomic layers depth/height with respect to an average surface occur. The perfect contact and sticking of the glue to the Ge sample excludes that such a roughness would be due to the removal of the very top atomic Ge layers by the Ar ion bombardment during the sample preparation. The Ge lattice terminates fully crystalline without any dislocations in the subsurface region.

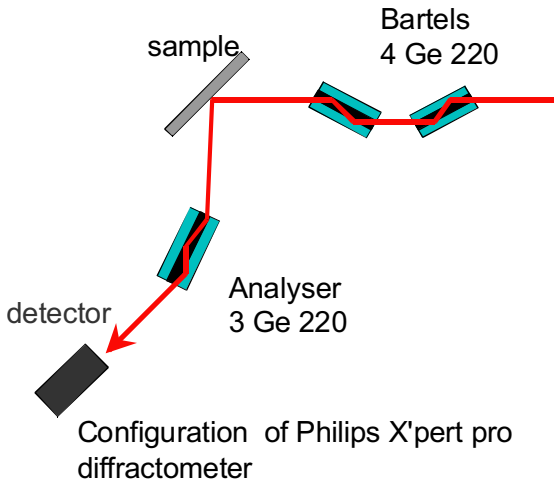

Figure 2. RSM setup. High-resolution Philips diffractometer with a 3 bounce analyser crysta was used.

Figure 3. Artificial Ge channel-cut monochromator (assembled, glued together). The red arrow shows the machined inner side.

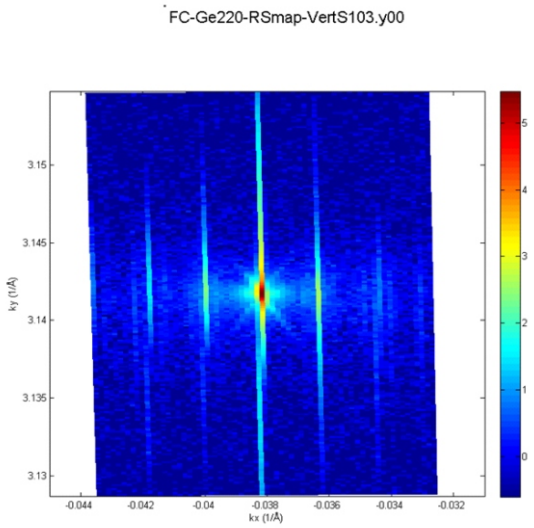

Figure 4. The reciprocal space map shows vertical lines with a spacing 1.51 $^{-3}$ Å^{-1} corresponding to a planar spacing of 416 nm.

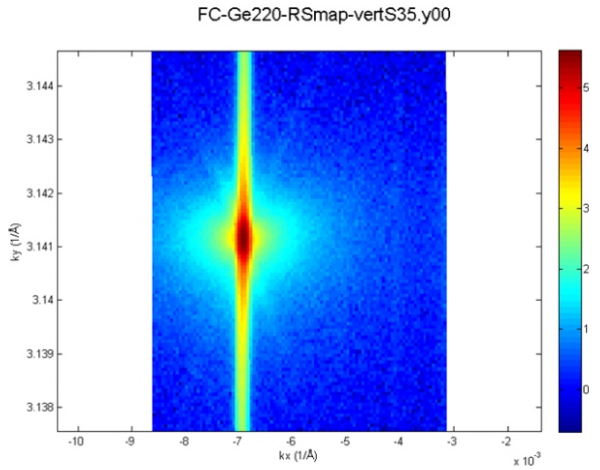

Figure 5. RSM shows suppression of truncation rods present in Fig. 4. The diffuse scattering is present but limited.

only flat but also curved or free-form surfaces with very high accuracy. A high planarity of the diffraction surface down to 3nm/50µm has been achieved. This is very important due to a very small incidence or emergence angles of the hard X-ray beam in highly asymmetric channel- cut X-ray crystal monochromators [3].

1. G.M. Robinson, M.J. Jackson: A review of micro and nanomachining from a materials perspective, Journal *of Materials Processing Technology,* Volume **167**, Issues 2–3, 30 August 2005, Pages 316–337.
2. Robert E. Parks: Fabrication of infrared optics*, Optical Engineering* **33**(3), 685—691 (March 1994).
3. C. Ferrari et al.: X-ray diffracted intensity for double-reflection channel-cut Ge monochromators at extremely asymmetric diffraction conditions*, J. Appl. Crystallogr.* **44**, 353–358 (2011).

This work was done within Research and Development Centre for Advanced X-ray Technologies, ITMS code 26220220170, supported by the Research and Development Operational Program funded by the ERDF (0.5). This work was supported also by the Slovak Research Agency under the contracts No. APVV-14-0745 and Scientific Grant Agency of the Ministry of Education of Slovak Republic and the Slovak Academy of Sciences, project No. VEGA-2/0004/15.

L17

EVALUATION OF THREADING DISLOCATION DENSITY IN III-NITRIDE EPITAXIAL LAYERS

E. Dobročka

Institute of Electrical Engineering, Slovak Academy of Sciences, Dúbravská cesta 9,841 04 Bratislava, Slovak Republic
edmund.dobrocka@savba.sk

The III–nitride semiconductors of AlN, GaN, and InN and their ternary alloys have great potential for use in optoelectronic and high-temperature electronic devices due to their wide range of bandgaps and high-temperature stability. The increasing range of their applications such as light emitting diodes, lasers and high power transistors requires the study of the influence of extended defects on the electrical and optical properties of these materials [1, 2]. The most important defects in the structures are threading dislocations (TDs). Their total density in the epitaxial layers varies in the range from 10^8 to 10^{10} cm^{-2}. They are predominantly oriented perpendicularly to the sample surface as is proved by transmission electron microscopy (TEM) observations. Three types of dislocations are generally reported in these materials: a-type edge dislocations with the Burgers vectors $\vec{b}_e$ $1/3\langle 11\bar{2}0\rangle$, c-type screw dislocations with $\vec{b}_s$ $\langle 0001\rangle$ and mixed (a + c)-type dislocations with $\vec{b}_m$ $1/3\langle 11\bar{2}3\rangle$. The density of edge dislocations, that are responsible for lattice twisting within the plane of the sample, exceeds the density of screw and mixed dislocations causing the lattice tilt out of the plane of the layer.

The dislocation density can be measured directly by TEM, but the accuracy is rather poor due to the limited area covered by TEM micrographs. The main significance of this technique is the possibility of determining the type of the dislocations as well as the kind of their arrangement. Alternatively, X-ray diffraction can be used to detect the lattice distortions caused by the presence of dislocations averaged over a sufficiently large sample area. The effect of lattice distortions on the diffraction peak broadening is well known and there is a vast amount of literature dealing with this topic. While the widths of the peaks can be measured by various X-ray diffraction techniques and evaluated by fitting to different types of model curves, their interpretation in terms of dislocation density is not straightforward. As regards the measuring techniques, there is an important difference between polycrystalline and single crystalline (epitaxial) samples. While in the former case a large number of diffractions can be measured within one powder diffraction pattern recorded e. g. in Bragg-Brentano set-up, measuring of (001) oriented single crystals in symmetric configuration provides only diffractions that are sensitive to lattice tilt and can therefore reveal only the presence of screw (eventually screw component of mixed) TDs. The edge dislocations influence the lattice planes perpendicular to the surface and measuring the corresponding diffractions requires the grazing incidence set-up.

An alternative skew geometry enabling to utilize the widths of diffractions that are inclined by an angle with respect to surface normal was proposed by Sun et al. [3] and Lee et al. [4]. Their approach is based on the model that supposes a mosaic structure of epitaxial films having a large lattice mismatch [5]. The width of the diffraction is given as

$$ {}^{n}_{hkl} \quad (\ {}_{0}\cos \ )^{n} \quad (\ {}_{90}\sin \ )^{n} \quad (2 \ / L)^{n} / K^{n}_{hkl} \qquad (1) $$

where $_0$ and $_{90}$ are the FWHMs of the diffractions and , respectively, L is the lateral domain size and K_{hkl} is the magnitude of the diffraction vector. The exponent n varies between 1 (Lorentzian intensity profile) and 2 (Gaussian profile). The third term in (1) corresponds to the size broadening effect that in some cases has to be taken into account.

Measuring of at least one symmetric (at $=0$) and one skew diffraction at enables one to obtain the extrapolated value of $_{90}$ corresponding to twist of the mosaic blocks due to the presence of edge TDs.

In the vast majority of analyses of the quality of epitaxial layers the formulas originally derived for polycrystalline metallic samples are used for evaluation of the TDs densities from the diffraction peak widths [6-8]. Two limiting cases are distinguished: (i) random distribution of TDs, in which the dislocation density is related to peak width as

$$ {}^{rand} \quad \frac{{}^{2}}{2 \ \ln 2b^{2}} \qquad (2) $$

and (ii) correlated distribution when the dislocations are localized at the boundaries of mosaic blocks

$$ {}^{corr} \quad \frac{}{\sqrt{2 \ \ln 2}bL} \qquad (3) $$

where b is the magnitude of Burgers vector and L is the average size of the blocks. It is worth noting that for polycrystalline samples the formulas (2) and (3) do not provide the possibility to distinguish between screw and edge dislocations. In order to solve this problem more sophisticated approaches are required [9, 10] that take into consideration the mutual orientation of the dislocation line, possible Burgers vectors and diffraction vectors and eventually the crystal anisotropy. These complications are considerably reduced for epitaxial layers, where only one direction of TDs and, in principle, only two types of Burgers vectors have to be considered. Setting the values of $_0$

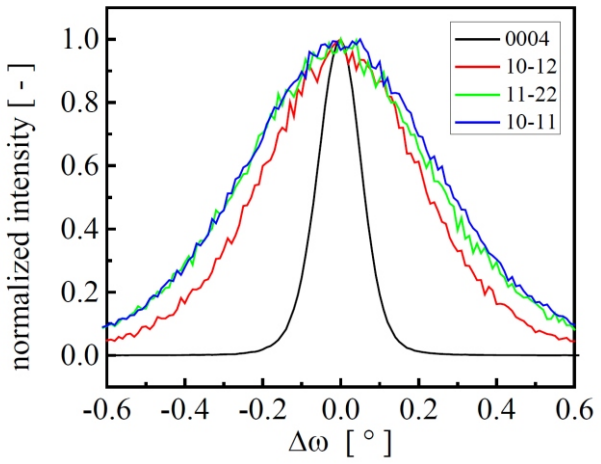

Figure 2. Normalized X-ray rocking curves of selected diffractions of InN.

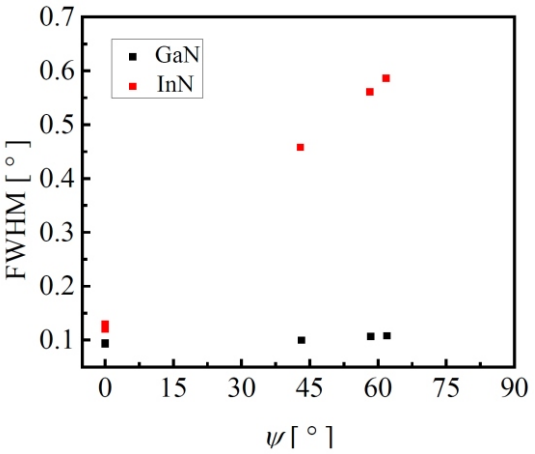

Figure 3. Dependence of FWHMs of rocking curves on the tilting angle .

and $_{90}$ for the peak widths in (2) or (3) and using the appropriate magnitudes of Burgers vectors b_s and b_e , one can easily calculate the density of screw and edge dislocations. The results evidently depend on the supposed dislocation arrangement that has to be verified e. g. by TEM observation along with the estimation of the parameter L.

More precise approach based on the analysis of the shape of the rocking curves was proposed by Kaganer and co-workers [11, 12]. They fit the measured intensities by the numerical Fourier transformation of the correlation function proposed by Krivoglaz [9] in the whole range of rocking curves including the peak tails. In addition to dislocation density, the model allows to extract also the so called cut-off radius R_c. This parameter was introduced by Wilkens [12] in order to characterize the correlation of dislocations within the framework of "restricted random distribution" model. Its value gives the size of the domains within which the dislocation distribution is random (the sum of all Burgers vectors in the domain is zero). However, the application of this model is rather laborious and not suitable for everyday use by technologists. For practical purposes approximate formulas were derived on the basis of this model [11] in the forms

$$_e \quad \frac{18 \ _{90}^2 \cos^2 \ _B}{(2.8 \quad \ln M)^2 b_e^2} \tag{4}$$

for edge dislocation and

$$_s \quad \frac{36 \ _0^2}{(2.4 \quad \ln M)^2 b_s^2} \tag{5}$$

for screw ones. $_B$ is the Bragg angle of the measured diffraction and the dimensionless parameter $M = R_c \ _i$ depending on the corresponding TDs densities $_i$ varies between 1 and 2. Surprisingly, compared to (2), these equations result in four times higher edge dislocation density and an order higher screw dislocation density [11].

It is seen that there is a large discrepancy between different approaches to the evaluation of TDs densities. While the dependence $^2 / b^2$ for random distribution is generally accepted, the numerical factor can considerably vary, eventually depends on dislocation densities. This uncertainty can be partially excluded by comparison of the results with the TEM observation, although the precision of dislocation density measurement by TEM is rather low. Once the ratio $_{XRD}/ \ _{TEM}$ is established for a given type of epitaxial system (and eventually laboratory), the calibration can be used for further XRD analyses. This procedure was applied for the evaluation of TDs in InN layers grown on GaN [13]. The densities of both screw and edge TDs were calculated according to

$$\frac{^2}{1.88 b^2} \tag{6}$$

where 1.88 is the calibration constant obtained from the comparison with TEM.

In this contribution the TDs density was evaluated in both layers of InN/GaN/sapphire(0001) sample. The InN and GaN layers were 0.5 m and 0.3 m thick, respectively. The details of the growth procedure are described elsewhere [14]. High resolution X-ray diffraction analysis was carried out using Bruker D8 DISCOVER diffractometer equipped with X-ray tube with rotating Cu anode operating at 12 kW. The measurements were performed with parabolic Goebel mirror and four-bounce Ge 022 Bartels monochromator in the primary beam. All diffraction curves were recorded in an open detector mode. The InN layer on GaN was fully relaxed as confirmed by measuring of one asymmetric $11\bar{2}4$ diffraction. The density of dislocations with screw and edge components in both InN and GaN layers was evaluated from the X-ray rocking curves. FWHMs of two symmetric diffraction – 0002, 0004 and three skew ones – $10\bar{1}2, 11\bar{2}2, 10\bar{1}1$ were determined. Four of them are shown for InN layer in Fig. 1. Comparison of the peak widths of the same diffractions for InN and GaN are shown in Fig. 2. It is seen that for InN layer the peak broadening systematically increases with the tilting angle indicating that the density of edge TDs exceeds the density of screw ones. On the contrary, the peak widths practically do not change for GaN layer.

The TDs densities $_s$ and $_e$ were calculated according to (6), where the FWHMs of rocking curves $_0$ and $_{90}$ at the inclination angle $= 0$ and at the extrapolated value

= 90 were set for the parameter . Gaussian type of rocking curves was supposed, hence the exponent $n = 2$ was used in (1) for calculation of $_{90}$. The size effect (third term in (1)) was neglected in the calculation. The values of the tilting angle for skew diffractions were calculated from the lattice parameters of InN (PDF 00-050-1239) and GaN (PDF 00-050-0792). The magnitudes of Burgers vectors b_s and b_e are equal to the lattice parameters c and a, respectively, for both hexagonal materials.

The obtained TDs densities are
$^{InN}_{s}$ 7.2 10^8 cm $^{-2}$, $^{InN}_{e}$ 5.6 10^{10} cm $^{-2}$,
$^{GaN}_{s}$ 5.4 10^8 cm $^{-2}$ and $^{GaN}_{e}$ 1.9 10^9 cm $^{-2}$.

For both layers the same value 1.88 of the calibration constant was used in (6). Generally, one should be cautious with the choice of calibration proposed by different authors. The ratio $_{XRD}/_{TEM}$ may vary significantly from 0.1 to 7 as summarized in [4]. But in spite of this uncertainty, the increase of the density of edge TDs in the InN layer in comparison to GaN is evident. While the density of screw dislocations is practically the same, new edge TDs are generated during the growth of InN layer and their density exceeds the density of edge TDs "coming" from GaN layer by more than one order of magnitude. This is probably caused by large mismatch between the GaN and InN lattices that is ~ 10% for fully relaxed InN layer.

The analyzed samples were rather thick and the corresponding diffractions of InN and GaN were well separated even in the skew geometry used in the experiment. This is due to the large difference between the lattice parameters of these materials. However, one can encounter some difficulties when attempting to measure the TDs densities in multilayered ternary compounds having similar lattice parameters. The use of analyser crystal instead of open detector system can improve the resolution, however, this modification can seriously decrease the intensity. This is particularly important if the measurement should be performed on samples with the layer thicknesses in the range of tens of nanometers. These values are typical for up-to-date technologies. As regards the calculated TDs densities, one should reconcile oneself to the fact that the precision of density evaluation is seriously limited. This is not caused by the possible error of measurement but is rather a consequence of the fact that each model intended to describe the dislocation distribution is too far from reality.

1. S. C. Jain, M. Willander, J. Narayan, J. Appl. Phys., **87**, (2000), 965.
2. W. V. Lundin, A. E. Nikolaev, A. V. Sakharov, S. O. Usov, E. E. Zavarin, P. N. Brunkov, M. A. Yagovkina, N. A. Cherkashin, A. F. Tsatsulnikov, Semiconductors, **48**, (2014), 53.
3. Y. J. Sun, O. Brandt, T. Y. Liu, A. Trampert, K. H. Ploog, Appl. Phys. Lett. **81**, (2002), 4928.
4. S. R. Lee, A. M. West, A. A. Allerman, K. E. Waldrip, D. M. Follstaedt, P. P. Provencio, D. D. Koleske, and C. R. Abernathy, Appl. Phys. Lett. **86**, (2005), 241904.
5. V. Srikant, J. S. Speck, D. R. Clarke, J. Appl. Phys. **82**, (1997), 4286.
6. P. Gay, P. B. Hirsch, A. Kelly, Acta Metall. **1**, (1953), 315.
7. C. G. Dunn, E. F. Koch, Acta Metall. **5**, (1957), 548.
8. R. Chierchia, T. Böttcher, H. Heinke, S. Einfeldt, S. Figge, D. Hommel, J. Appl. Phys. **93**, (2003), 8918.
9. M. A. Krivoglaz, *X-ray and Neutron Diffraction in Nonideal Crystals.* Berlin: Springer-Verlag, 1996.
10. R. Kužel, Z. Kristallogr. **222**, (2007), 136.
11. V. M. Kaganer, O. Brandt, A. Trampert, and K. H. Ploog, Phys. Rev. B,**72**, (2005), 045423.
12. V. S. Kopp, V. M. Kaganer, M. V. Baidakova, W. V. Lundin, A. E. Nikolaev, E. V. Verkhovtceva, M. A. Yagovkina, N. Cherkashin, J. Appl. Phys. **115**, (2014), 073507.
13. C. S. Gallinat, G. Koblmüller, Feng Wu, J. S. Speck, J. Appl. Phys. **107,** (2010), 053517.
14. Ch. Zervos, A. Adikimenakis, P. Beleniotis, A. Kostoupolos, M. Kayambaki, K. Tsagaraki, G. Konstantinidis, A. Georgakilas, Appl. Phys. Lett. **108**, (2016), 142102.

The author gratefully acknowledges A. Georgakilas and A. Adikimenakis from FORTH, Greece for providing the sample.

L18

COMPOSITION AND STRAIN DETERMINATION OF (Al,Ga)N ALLOY FILMS

O. Caha[1,2], P. Kostelník[3], T. Novák[3]

[1]CETEC MU, Masaryk University, Kotlářská 2, 611 37 Brno
[2]Faculty of Science, Masaryk University, Kotlářská 2, 611 37 Brno
[3]ON Semiconductor Czech republic, Rožnov pod Radhoštěm
caha@physics.muni.cz

Wide band gap semiconductors are widely used for blue LEDs in a modern light production. They are also of growing interest for high voltage power applications where high charge carrier mobility and electric field strength allows better high frequency performance of electronic devices than standard silicon technology. LED technology often use sapphire (0001) substrates. Our goal is to develop GaN growth technology using cheaper and easier available silicon (111) substrates.

As a part of those studies we have grown series of samples (Al,Ga)N/AlN ternary alloy layers on silicon (111) substrate within a full concentration range, i.e from pure

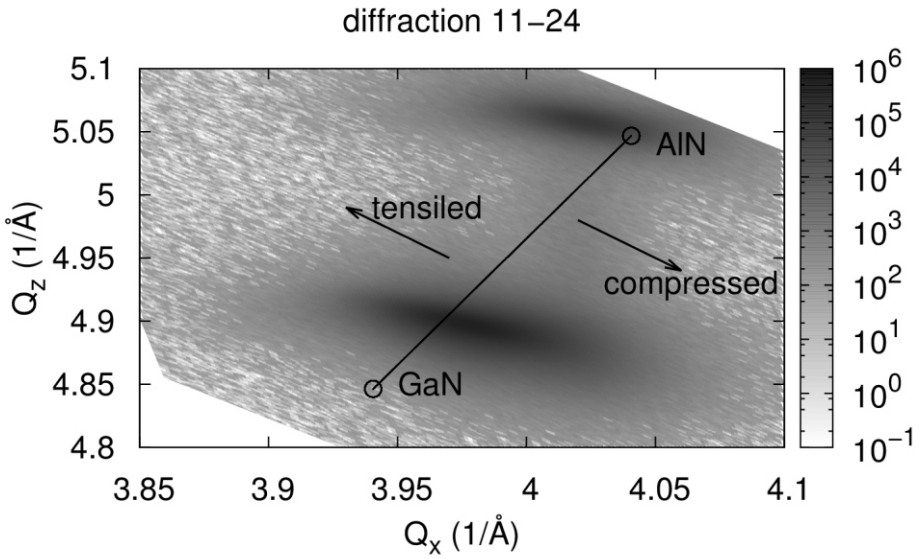

Figure 1. Representative reciprocal space map in the vicinity of 1124 reciprocal lattice point. The line represents position of an unstrained (Al,Ga)N alloy peaks with emphasized points corresponding pure AlN and GaN.

AlN to GaN. Such series allowed a systematic study of the concentration dependence of the wurtzite lattice parameters, band gap, and phonon frequencies.

The measurement were performed in a couple of diffractions, typically 0004 and 1124 as a symmetric and asymmetric diffraction. A representative reciprocal space map in the vicinity of 1124 reciprocal lattice point is plotted in figure 1.

The concentration dependence of the lattice parameter was determined assuming linear Vegard's law in both *a* and *c* hexagonal lattice parameters [1].

$$a(x) \quad 0.31862(1 \quad x) \quad 0.31106x \ [nm] \qquad (1)$$
$$c(x) \quad 0.51855(1 \quad x) \quad 0.4979x \ [nm] \qquad (2)$$

We have tested the linear dependence of the (Al,Ga)N alloy using energy dispersive X- ray spectroscopy (EDXS) in scanning electron microscope with electron beam voltage of 4 keV, which does not penetrate below the (Al,Ga)N layer. The results are are shown in figure 2 and shows a good agreement within precision of 0.015 in chemical composition.

The x-ray diffraction allows us to *decouple* chemical composition with a reasonable precision of 0.01 and strain of all the layers in the structure. Therefore, X-ray diffraction was used as a primary reference method to determine (Al,Ga)N alloy composition. The layers were studied also using a couple of optical spectroscopic methods, especially VIS-UV reflectometry and Raman scattering. The advantage of the optical methods is speed and possibility of wafer mapping. On the other hand those methods lacked proper calibration and the concentration information is also affected by a strain. The calibration curves of optical band gap and Raman phonon frequencies are reported [2].

1. H. Jiang, G. Y. Zhao, H. Ishikawa, T. Egawa, T. Jimbo, M. Umeno, *Journal of Applied Physics* **89,** 1046 (2001).
2. C. Wang, O. Caha , F. Münz, P. Kostelník, T. Novák, J. Humlíček, *Appl. Surf. Sci.*, in press.

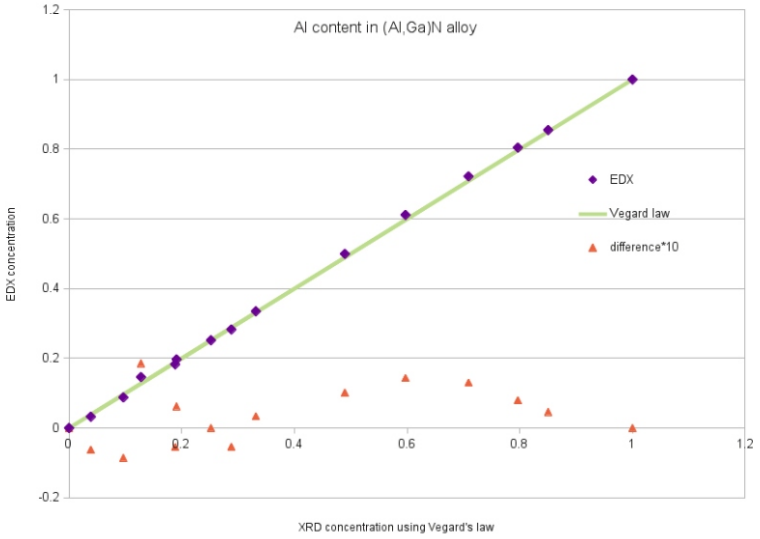

Figure 2. Chemica composition of (Al,Ga)N alloy determined using EDS plotted with respect to the chemical composition determined using Vegard's law from XRD data.

L19

FeMnGa AND NiMnGa ALLOYS IN THE LIGHT OF THE DIFFRACTION AND MICROSCOPY TECHNIQUES

J. Kopeček[1], K. Onderková[1], D. Král[2], L. Klimša[1], L. Straka[1] and O. Heczko[1]

[1]*Department of Functional Materials, Academy of Sciences of the Czech Republic, Institute of Physics, Na Slovance 2, CZ-18221 Prague, Czech Republic*

[2]*Department of Physics of Materials, Institute of Physics of Charles University, Ke Karlovu 5, CZ-12116 Prague 2, Czech Republic*

Whereas NiMnGa ferromagnetic shape memory alloys became an icon of the field in the last two decades, FeMnGa alloys are still waiting for exploration. There are several expectations. Heusler type alloy Fe_2MnGa is one of the few compounds exhibiting ferromagnetic shape memory effect, i.e. reversible martensitic and ferromagnetic transformation in response to the magnetic field (beyond conventional response to temperature or mechanical stress) [1-2]. Multiferroic behavior in this system is connected with interesting magneto-transport and magneto-optic properties [3-4]. Since couple of presentation is dedicated to NiMnGa system - even from the same site, let switch our attention in this article to "poor relative" FeMnGa. It is known that the magnetic moment strongly depends on Fe content or Fe/Mn ratio, and the ordering varies from ferromagnetic to antiferromagnetic or paramagnetic.

To open an investigation of this system in our laboratory, we prepared a wide set of samples covering a wide surroundings of the stoichiometric Heusler alloy (Fe_2MnGa). All samples were metallographically prepared and conventionally studied using LOM, SEM and its hyphenated analytical techniques energy-dispersive X-ray spectrometry (EDS) and electron backscatter diffraction (EBSD). The crystallographic structures were analysed by X-ray diffraction (XRD) to obtain information on the structures present in the samples, because there are doubts about the high-temperature phase structure, i.e., whether it is $D0_3$ [3] or $L1_2$ [5], see Fig. 1.

The structural studies were found to be complicated as proper lattice parameters are not known and good polycrystals are not yet available. Thus only the rough estimate of the presented phases will be presented. Peculiarities of structure and microstructure found during investigation will be presented in the lecture, e.g. as in $Fe_{40}Mn_{25}Ga_{35}$ alloy in Fig. 2, where tetragonal $L1_0$ a cubic $D0_3$ structures are presented.

Apart from structural investigation, the functional properties of the samples were measured: magnetic properties by vibration magnetometer, and magneto-optic properties by ellipsometry. Saturated magnetization sharply grows, when iron content overcomes approx. 30 at. %, and nearly immediately drops above 50 at. % of iron in alloys with 25 at.% manganese content. We can speculate about transition from ferromagnetic to antiferromagnetic state in these samples. The investigated FeMnGa samples exhibit magneto-optical spectra similar to those of pure Fe or some Fe compounds, suggesting higher contribution of free electrons to their magneto-optical properties compared to NiMnGa. The amplitude of Kerr effect scales with composition similarly as the saturation magnetization. At room temperature the amplitude of magneto-optical effect of ferromagnetic alloys was approximately five times higher than for off-stoichiometric Ni-Mn-Ga allowing observation of magnetic domains by Kerr effect. The striking difference between magneto-optical spectra of Fe-Mn-Ga and Ni-Mn-Ga suggest that the mechanism of martensitic transformation might be different in these systems [6] despite the same Heusler type.

This work was supported in part by the MEYS CR FUNBIO CZ.2.16/3.1.00/21568 (SEM purchase), LO1409 and LM2015088 projects (SEM maintenance) and CSF project 14-36566G (AdMat).

1. Omoti T, *et al.* 2009 *Appl. Phys. Lett.* **95** 082508.
2. Zhu W, *et al.* 2009 *Appl. Phys. Lett.* **95** 222512.
3. Kudryavstev Y V, *et al.* 2012 *Acta Mater.* **60** 4780.
4. Khovaylo V V, et al. 2013 Phys. Rev. B 87 174410.
5. Gasi T, et al. 2013 J. Appl. Phys. 113 17E301.
6. Heczko O 2014 Mater. Sci. Technol. 30 1559.

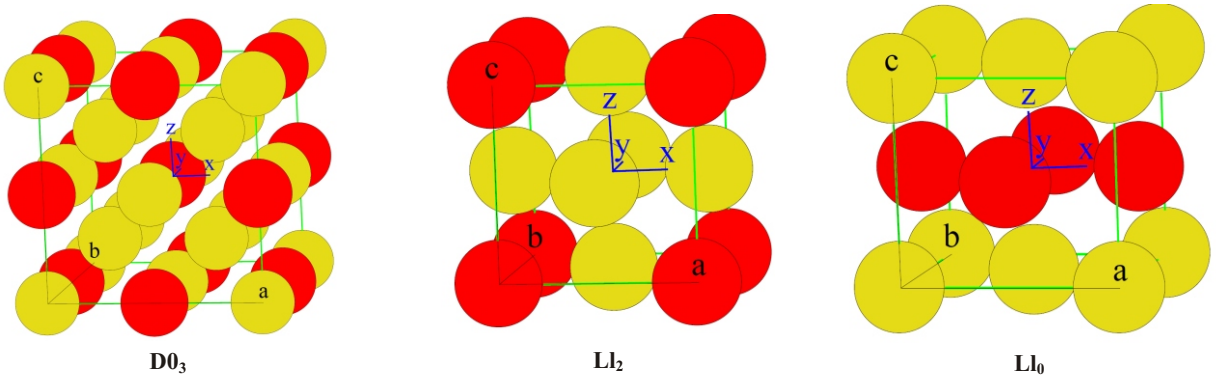

Figure 1. Structures in the system Fe – Mn – Ga. Fe - yellow (light), Mn, Ga - red (dark).

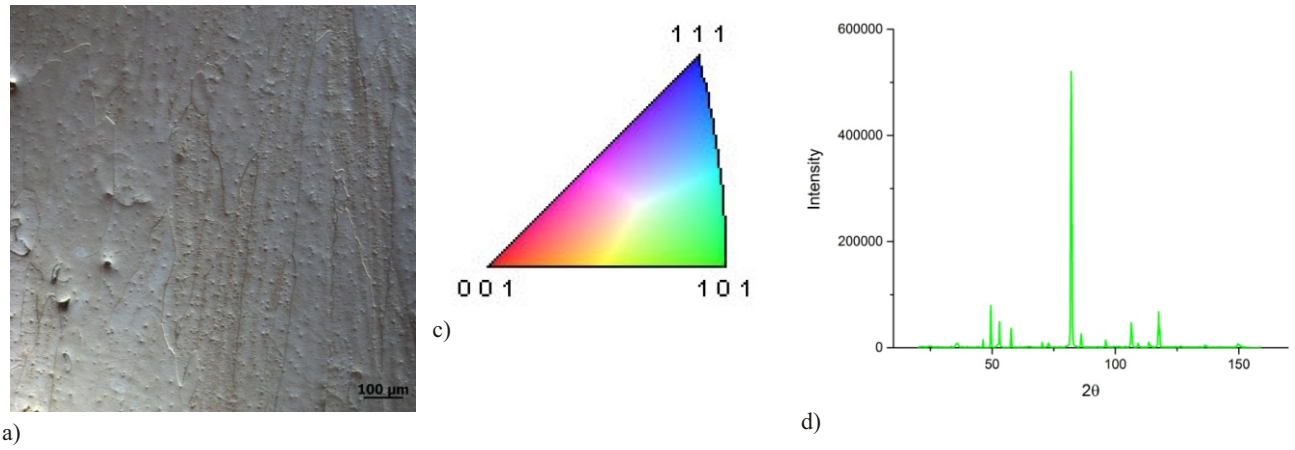

Figure 2. $Fe_{40}Mn_{25}Ga_{35}$ alloy; a) optical microscopy; EBSD orientation map, visible are cubic $L1_2$ grain, whereas tetragonal $L1_0$ grains are black as evaluation quality was poor due to the misfit in *c/a* ratio; c) scale orientation in EBSD map; d) summarized diffraction pattern from large grain material. The summation over rotated and inclined sample was applied, but it was found insufficient for finding proper tetragonal lattice parameters.

Session VII, Tuesday, June 20, afternoon

L20

STRUCTURAL EVOLUTION OF Ta-ALLOYED Ti-Al-N HARD COATINGS

T. Roch, M. Janík, M. Mikula, M. Truchlý, D. Plašienka, M. Pleva, P. Kúš

Department of Experimental Physics, Faculty of Mathematics Physics and Informatics,Comenius University in Bratislava, Mlynska Dolina, 842 48 Bratislava, Slovakia

roch@fmph.uniba.sk

Well known Ti-Al-N hard coatings commercially used for abrasive wear protection in machine industry exploit combination of extreme hardness with good oxidation resistance. But inherent brittleness limits their applications. In general, hard coatings have to show high toughness, elasticity and good adhesion to substrate, while keeping hardness and thermal stability at reasonable levels. Enhancement of toughness in terms of ductility increase was predicted for TiAlN (cubic B1) alloyed with transition metal, with best results for Ta, Mo and W [1]. Compelling improvements were predicted by numerical simulations and some experiments by means of low tantalum alloying ($y <$ 0.1) of $Ti_{1-x-y}Al_xTa_yN$ coating material [2,3]. Hardness increased up to 40 GPa and spinodal decomposition process shifted from 900 °C to 1200 °C.

Here, we investigated this material with even higher Ta content *y*. Our aim was the detailed X-ray diffraction structural analysis of $Ti_{1-x-y}Al_xTa_yN$ (TATN) coatings as-deposited on monocrystalline Si (001), Al_2O_3 (0001) and on polycrystalline tungsten carbide substrates with $y = 0$ - 0.6. Deposition was performed using reactive unbalanced DC magnetron co-sputtering from TiAl and Ta tilted targets in a flowing Ar + N_2 mixture atmosphere at 0.5 Pa. Samples were mounted on the heated holder at different positions with respect to the targets, yielding different Ta content in TATN thin films. The chemical elemental composition determined by energy dispersive spectroscopy showed monotonic increase of Ta content with the decrease of (sample, Ta-target) distance.

The XRD analysis involved microstructure determination, texture specification by pole figures measurement and residual stress analysis using $\sin^2$ method. Figures 1a and 1b show measurements of area maps with combined 2 -scans at varying tilt positions of sample without Ta (TiAlN) and sample with higher Ta content ($y = 0.46$), respectively. These patterns show very clearly presence of various structural effects together. With increasing tantalum content, the phase remains cubic NaCl type, the lattice parameter increases and coherent domain size decreases. Regardless of substrate type in all coatings the texture evolves from 111 (for $y = 0$) to 001 orientation with increasing *y*. Polar figures in 111 reflection show presence of